JOURNAL OF PHYSICAL ORGANIC CHEMISTRY
J. Phys. Org. Chem. 2002; **15:** 431–447
Published online in Wiley InterScience (www.interscience.wiley.com). DOI: 10.1002/poc.495

Review Commentary

Mechanism and dynamics of organic reactions: 1,2-H shift in methylchlorocarbene†

Elfi Kraka and Dieter Cremer*

Department of Theoretical Chemistry, Göteborg University, Reutersgatan 2, S-41320 Göteborg, Sweden

Received 4 September 2001; revised 23 January 2002; accepted 6 February 2002

ABSTRACT: The unified reaction valley approach (URVA) was used to investigate the mechanism of the rearrangement of methylchlorocarbene to chloroethene [reaction(1)] in the gas phase with special emphasis on the role of H tunneling. The reaction valley of (1) was explored using different methods (HF, MP2 and DFT/B3LYP) and different basis sets [6–31G(d), 6–31G(d,p) and cc-pVTZ]. Results were analyzed characterizing normal modes, reaction path vector and curvature vector in terms of generalized adiabatic modes associated with internal parameters that are used to describe the reaction complex. For reaction (1), H tunneling plays a significant role even at room temperature, but does not explain the strongly curved Arrhenius correlations observed experimentally. The probability of H tunneling can be directly related to the curvature of the reaction path and the associated curvature couplings. The reaction is preceeded in the forward and reverse direction by energy-consuming conformational changes that prepare the reactant for the actual 1,2-H shift, which requires only little energy. The effective energy needed for CH bond breaking is just 6 kcal mol^{-1} for (1). The gas-phase and the solution-phase mechanisms of (1) differ considerably, which is reflected by the activation enthalpies: 11.4 (gas, calculated) and 4.3 kcal mol^{-1} (solution, measured). Stabilizing interactions with solvent molecules take place in the latter case and reduce the importance of H tunneling. The non-linearity of the measured Arrhenius correlations most likely results from bimolecular reactions of the carbene becoming more important at lower temperatures. Copyright © 2002 John Wiley & Sons, Ltd.

KEYWORDS: carbene rearrangement; H shift; reaction mechanism; H tunneling; reaction valley; reaction path Hamiltonian; methylchlorocarbene

INTRODUCTION

Recently, we investigated the mechanism and dynamics of substitution and cycloaddition reactions using the unified reaction valley approach (URVA).[1–4] URVA is based on the reaction path hamiltonian (RPH) of Miller *et al.*,[5] the intrinsic reaction coordinate (IRC) of Fukui[6,7] and the generalized adiabatic mode concept of Cremer and co-workers[8,9] URVA was developed to study the mechanism of a chemical reaction in detail. For this purpose, the reaction path embedded in the reaction valley is explored from the location of the minimum associated with the reactants to the first-order saddle point being the position of the transition state (TS) and to the minimum associated with the products. During this journey all changes in the physical and chemical properties of the reaction complex (RC, the supermolecule made up from the reacting molecules) are monitored so that a detailed account of the reaction mechanism can be given.[1–4]

The direction and the curvature of the reaction path provide important information on the latter. In previous work, we found that bond breaking and bond forming are indicated by a strong curvature of the reaction path. Based on the sequence and the position of the curvature peaks, a TS region, in which the chemical processes occur, can be distinguished from van der Waals and preparation regions, in which the first interactions of the reaction partners develop and in which the reactants prepare for the actual chemical processes.[1,2,4] The van der Waals region can be located even if a van der Waals complex does not exist on the potential energy surface (PES). The position of the energy TS in the transition state region (early or late) is in line with the Hammond postulate indicating an exothermic or endothermic reaction. The height of the curvature peaks can be related to the strength of the bonds being broken/formed, which has an influence on the reaction barrier and the reaction energy.[1,2] Finally, it is possible to detect hidden inter-

**Correspondence to:* D. Cremer, Department of Theoretical Chemistry, Göteborg University, Reutersgatan 2, S-41320 Göteborg, Sweden.
†Presented in part at the 8th European Symposium on Organic Reactivity (ESOR-8), Cavtat (Dubrovnik), Croatia, September 2001.
Contract/grant sponsor: Swedish Natural Science Research Council (NFR).

mediates along the reaction path by relating curvature and other features of the path to structural changes of the reaction complex. Hidden intermediates are transient structures with unique electronic and structural features but which do not occupy a distinct stationary point on the PES. However, they possess electronic features that by variation of the conditions of a reaction (solvent, temperature, substituent influence, etc., which imply a change in the PES) lead to a true intermediate occupying a local minimum.[4] In this way, hidden intermediates present an important mechanistic link between different reaction mechanisms observed for different environmental conditions or substitution patterns.

The curvature of the reaction path is related to the curvature couplings, which result from a coupling between the vibrational modes orthogonal to the reaction path and the translational mode of the RC along the reaction path. They provide information how energy can be transferred from vibrational modes into the reaction path mode and vice versa.[10,11] Knowledge of the curvature couplings can be used for mode selective rate enhancement. Similarly, a coupling between vibrational modes along the reaction path leads to energy dissipation during the reaction.

In previous work, we investigated exclusively bimolecular reactions, in which the chemical processes involve two different molecules. The chemical processes could be easily located by the curvature of the reaction path and the mechanism (sequence of bond breaking/forming processes) identified. This is also the case for other reactions investigated with the reaction path hamiltonian.[11] Only a few unimolecular reactions were investigated, but in none of these cases was it possible to determine the reaction path curvature and to carry out a mechanistic analysis.[12,13]

In this work, we investigated for the first time the mechanistic details of an unimolecular reaction using URVA. As an example, the 1,2-H shift in singlet methylchlorocarbene leading to vinyl chloride was analyzed [reaction (1), Scheme 1(a)][14–18] where results are related to the corresponding arrangements of other carbenes, in particular that of benzylchlorocarbene to (*Z*)-and (*E*)-*β*-chlorostyrene [reactions (2a) and (2b), Scheme 1(a)].[19–25] These reactions can be considered as carbene self-insertions into an α-C—H bond with low activation energies and large exothermicity. Alternatively, one can speak of a hydride shift followed by the conversion of a zwitterionic singly bonded structure into a double bond structure [Scheme 1(b)]. The reaction is initiated by a hyperconjugative delocalization of the a C—H bonding electron pair into the empty pπ orbital at the carbene C atom. This requires that the C—H bond and pπ-orbital are properly aligned and that the σCH orbital energy is not too low.

LaVilla and Goodman[14] measured an Arrhenius activation energy E_a of 4.9 ± 0.5 kcal mol^{-1} (1 kcal = 4.184 kJ) ($\Delta H‡ = 4.3$ kcal mol^{-1}) and $\log A = 9.7 \pm 0.3$ ($\Delta S‡ = -16.1$ e.u.) for reaction (1) in heptane from 11 to 61 °C using time-resolved photoacoustic calorimetry. The low frequency factor suggested a highly ordered TS. Repetition of the measurement for a larger temperature range (−70 to 80 °C) in different solvents (heptane and 1,2-dichloroethane) with the help of nanosecond absorption spectroscopy in connection with the pyridinium ylide method led to curved Arrhenius plots and an inverse KIE (increasing k_H/k_D with increasing temperature *T*) which were related to either a branching of the reaction mechanism (the carbene is consumed by more than one reaction) or quantum mechanical tunneling.[15]

Calculations by Storer and Houk[17] seemed to confirm the latter assumption: Applying variational transition state theory (VTST) these authors calculated a rate constant of $k(1) = 1.7 \times 10^5$ s^{-1}; however, when including quantum mechanical tunneling via CD-SCSAG (centrifugal-dominant, small curvature, semi-classical, adiabatic, ground-state) theory obtained $k(1) = 1.35 \times 10^6$ s^{-1}, in perfect agreement with the experimental $k(1)$ value of 1.36×10^6 s^{-1} measured in heptane.[15] These calculations were based on an MP2/6–31G(d) PES traced out along the reaction path between 0.96 and

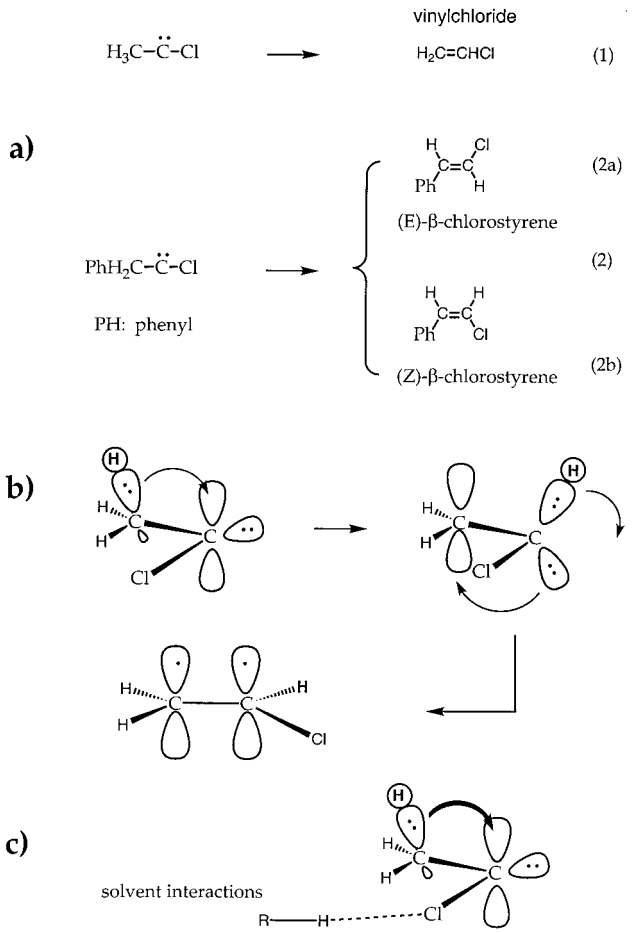

Scheme 1

0.84 amu$^{\frac{1}{2}}$ before and after the TS, respectively.[17] The corresponding barrier after zero-point energy (ZPE) corrections was found to be 12.6 kcal mol^{-1}, which reduced at MP4/6–311G(d,p)//MP2/6–31G(d) to 11.5 kcal mol^{-1} (Ref. 17; K. N. Houk, personal communication). Hence, the calculated activation energy was a factor of 2 larger than the measured value and despite this serious discrepancy the measured k value was reproduced when quantum mechanical tunneling was considered. Later calculations by Houk and co-workers[18] using DFT and other methods essentially confirmed the calculated activation energy which makes a $k(1)$ value of 10^4 s^{-1} much more likely than the experimental $k(1)$ of 10^6 s^{-1}.[15]

At this point one has to note that the quantum chemical calculations refer to the gas phase whereas the experiments were carried out in the solvent phase. Lavilla and Goodman[14] pointed out the influence of the solvent on the carbene stability and probably also on the TS. The second question concerns the sensitivity of the VTST results on the range investigated before and after the TS. Here, we will show that for an investigation of the reaction path in the full range from reactant to product in sufficiently small steps the influence of quantum mechanical tunneling is strongly reduced and the mechanism of the reaction in the gas phase differs considerably from that in the solution phase.

Experimental observations made for reaction (2) (Scheme 1) have been interpreted in a similarly contradictory manner as in the case of reaction (1). Liu *et al.*[22] carried out a laser flash photolysis investigation of 3-chloro-3-benzyldiazirine and 3-chloro-3-(phenyldideuteriomethyl)diazirine in isooctane over the range 60 to −80 °C, which led to curved Arrhenius plots for the 1,2-H and 1,2-D shifts in benzylchlorocarbene. The authors argued that quantum mechanical tunneling or solvent interactions are responsible for the observed kinetics. This interpretation was rejected by Merrer *et al.*,[23] who demonstrated by careful product analyses that rearrangement (2) is accompanied by intermolecular reactions of the carbene. Hence curved Arrhenius correlations do not necessarily implicate quantum mechanical tunneling. At low temperatures (−70 °C in 1,1,2,2-tetrachloroethane) no byproducts were observed for reaction (2) and a linear Arrhenius correlation resulted (E_a = 3.2 kcal mol^{-1}, log$A$ = 10.0 s^{-1}).[23]

In the last 5 years, the 1,2-H shift in various other carbenes was investigated,[25–28] benzylchlorocarbene was generated in a different way and the Arrhenius analysis for reaction (2) repeated[29] and solvent carbene interactions[30] and intermolecular reactions of the carbene were measured.[29,31–33] Although a number of alternative explanations of non-linear Arrhenius correlations were offered, the mechanism of the 1,2-H shift and, in particular, the role of quantum mechanical tunneling in this connection are not fully understood.

We will consider the mechanism and the dynamics of reaction (1) in the gas phase. In this connection we will discuss a number of questions: (1) what are the energetics of the reaction in the gas phase and do they differ from those in solution?; (2) is the mechanism shown in Scheme 1(b) (hydride transfer followed by double bond formation) a valid description for reaction (1); (3) do the bond breaking and bond forming processes occur exactly simultaneously or one after the other?; (4) can different stages of the reaction be distinguished as in the case of the substitution and cycloaddition reactions previously investigated?; (5) what structural changes initiate the reaction and how is it terminated and, what happens at the TS?; (6) is an enhancement of the reaction rate possible by pumping energy into a vibrational mode (mode selective rate enhancement)?; (7) 1,2-H shifts such as in reactions (1) and (2) are strongly exothermic: does energy dissipation occur along the reaction path or is the energy generated stored in the newly formed CH and CC double bond?; (8) what is the role of H tunneling, and can it be anticipated from the URVA analysis?; and (9) how does the environment influence the reaction mechanism?

We will proceed in the following way in subsequent sections to answer questions (1)–(9). First, we will briefly describe the theory of URVA and the computational methods used. The reaction path and reaction valley of rearrangement (1) will then be described. This is followed by a mechanistic and dynamic discussion, focusing in particular on the role of H tunneling and the influence of the environment.

THEORY AND COMPUTATIONAL METHODS

All structural changes of the RC can be described in a $3K$–L-dimensional configuration space (L-number of overall rotations and translations, K-number of atoms in the RC) spanned by the internal coordinates of the RC. In URVA, this space is partitioned into a one-dimensional reaction path space, along which the translational motion of the RC takes place, and a $(3K-L)-1$-dimensional orthogonal space, in which the transverse vibrations of the RC orthogonal to the motion along the reaction path occur. In URVA one follows the reaction path and calculates the harmonic vibrational modes of the RC along the path thus tracing out a harmonic $(3K-L)-1$-dimensional reaction valley with the reaction path being on the valley floor. URVA applied to the chlorocarbene rearrangement (1) required the following steps.

1. Calculation of the energy profile along the reaction path. The reaction path $\tilde{\mathbf{x}}(s)$ can be represented at a point $\tilde{\mathbf{x}}(s_0)$ as a Taylor series in s:[34,35]

$$\tilde{\mathbf{x}}(s) = \tilde{\mathbf{x}}(s_0) + \mathbf{t}(s)(s-s_0) + \frac{1}{2!}\mathbf{k}(s)(s-s_0)^2 + \dots \quad (1)$$

where s is the arc length of the path (reaction path length)

defined by the differential

$$ds^2 = d\mathbf{x}^\dagger \mathbf{M} d\mathbf{x} = d\tilde{\mathbf{x}}^\dagger d\tilde{\mathbf{x}} \quad (2)$$

and $\mathbf{M}$ is the diagonal matrix of nuclear masses. The reaction path $\tilde{\mathbf{x}}(s)$ is given by $3K$ mass-weighted Cartesian coordinates x_i of the RC for $s = 0 \rightarrow s$(reactant) or s(product) describing the steepest descent path from the TS toward reactant(s) and product(s). The first derivative of $\tilde{\mathbf{x}}(s)$ with regard to s is the reaction path vector $\mathbf{t}(s)$, which gives the direction of the path, while the second derivative of $\tilde{\mathbf{x}}(s)$ with regard to s is the reaction path curvature $\mathbf{k}(s)$. The reaction path is calculated by increasing (decreasing) the path length from $s = 0$ by suitable step sizes Δs (between 0.01 and 0.02 amu$^{\frac{1}{2}}$ bohr) until reactants or products are reached exploring the path by suitable path following algorithms.[2,10,11,34,35]

In this work, the reaction valley of (1) was described with the help of density functional theory (DFT).[36] DFT was employed in connection with the B3LYP hybrid functional[37] and the 6–31G(d,p) basis set.[38] The energetics obtained in this way for reaction (1) were verified by using the larger, more accurate cc-pVTZ basis set of Dunning.[39] The energetics of the reaction were also tested by carrying out second-order Møller–Plesset (MP2) perturbation theory calculations[40] employing the 6–31G(d,p) basis set. Finally, CCSD(T) calculations[41] with the 6–31G(d,p) basis were carried out to verify the energetics of reaction (1).

2. Calculation of all geometric changes along the reaction path. The internal coordinates q_n of the RC were calculated as functions of the path length s. As the changes of the geometry in the entrance channel are better described by the internal coordinates of the reactant whereas those in the exit channel of the reaction are better described by those of the product, a redundant coordinate set was used containing the internal coordinates of both reactant and product. We note in this connection that URVA uses adiabatic internal modes (AIMs), which are independent of the number of internal coordinates.[8,9]

3. Analysis of the reaction path direction. The reaction path vector $\mathbf{t}(s)$ was decomposed into basis vectors $\mathbf{u}_n(s)$:

$$\mathbf{u}_n(s) = \mathbf{M}^{-1}\mathbf{b}_n(s) \quad (3)$$

$$\mathbf{t}(s) = \sum_{n=1}^{3K-L} t_n(s)\mathbf{u}_n(s) \quad (4)$$

where an element i of $\mathbf{b}_n(s)$ is given by $\partial q_n(\mathbf{x})/\partial x_i$. The calculation of the coefficients $t_n(s)$ is described in Ref. 1. Vectors $\mathbf{u}_n$ in Eqns (3) and (4), which were first suggested by Kato and Morokuma,[35] represent the vibrational modes associated with the internal coordinates describing the RC.[1] Hence the movement along the reaction path is expressed in terms of internal coordinate modes $\mathbf{u_n}$(s), which are equivalent to the AIMs of Cremer and coworkers[8,9] used for the analysis of the normal mode vibrations (see points 5–7). For the analysis of $\mathbf{t}(s)$, the amplitude $A_{n,s}(\mathbf{t},s)$ of internal coordinate mode $\mathbf{u_n}$(s) given in Ref. 1 was used:

$$A_{n,s}(\mathbf{t},s) = \frac{[\mathbf{g}(s)^\dagger \mathbf{M}(s)^{-1}\mathbf{b}_n(s)]^2}{[\mathbf{g}(s)^\dagger \mathbf{M}(s)^{-1}\mathbf{g}(s)][\mathbf{b}_n(s)^\dagger \mathbf{M}(s)^{-1}\mathbf{b}_n(s)]} \quad (5)$$

[$\mathbf{g}(s)$-energy gradient at point s], which considers in addition to electronic effects the kinetic aspects of the translational motion along the reaction path.

4. Calculation of the forces exerted on the atoms of the RC along the reaction path. The energy gradient given as a function of s is analyzed in terms of forces associated with the internal coordinates. Since the internal coordinate, which dominates at a given point s_0 the direction of the reaction path, is known from step 3, the force having the strongest impact on the RC can be identified. Regions of repulsive (force >0) and attractive interatomic forces (<0) can be distinguished.

5. Calculation of the normal mode frequencies of the RC along the reaction path. For the description of the reaction valley, $N_{\text{vib}} = 3K - L - 1$ generalized normal modes $\tilde{\mathbf{l}}^g_\mu(s)$ and their associated frequencies $\omega^g_\mu(s)$ have to be calculated.[1,2,5,34,35] The harmonic reaction valley is given by

$$V(s,\mathbf{Q}) = V(s) + 1/2\sum_{\mu=1}^{N_{\text{vib}}} k^g_\mu(s)\cdot[Q^g_\mu(s)]^2 \quad (6)$$

where $k^g_\mu(s)$ is the generalized normal mode force constant, $Q^g_\mu(s)$ the generalized normal mode coordinate and $V(s)$ the energy profile along the reaction path. The normal mode frequencies $\omega^g_\mu(s)$ are plotted as a function of s, which provides a qualitative impression of the reaction mechanism and the mechanism of energy dissipation between the vibrational modes. A prerequisite for such an analysis is the correct resolution of all avoided crossings between vibrational eigenstates of the same symmetry along the reaction path. This implies mostly a reduction of stepsize Δs and the use of techniques such as the DMO procedure of Konkoli *et al.*[3] by which all avoided crossings of the vibrational eigenstates can correctly be resolved, and a reliable analysis of curvature coupling and mode–mode coupling coefficients (see steps 8 and 10) becomes possible.

Similar considerations will hold if the RC possesses C_1 symmetry because vibrational eigenstates may approach each other without crossing or they may cross exchanging

in the case of mode–mode coupling energy, which requires again an accurate resolution at crossing and non-crossing points.

6. Analysis of all normal modes in terms of adiabatic internal modes (AIMs). The AIMS are the vibrational modes of the internal coordinates and, by expressing normal modes in terms of AIMs, changes of the former can be directly related to structural changes of the RC. For example, the breaking of a bond leads to a strong decrease in the frequency of a normal mode, which in most cases increases again as soon as a new bond is formed. Decomposition of this normal mode into AIMs provides exact information as to where and how the bond breaking/forming process takes place.[1,2,4]

The determination and the advantages of AIMS are described elsewhere.[8,9] For URVA, generalized adiabatic internal modes $\mathbf{a}_n^g(s)$ are calculated in the $(3K-L)-1$-dimensional space. The properties of an $\mathbf{a}_n^g(s)$ mode are given by force constant $k_n^a(s)$, mass $m_n^a(s)$ and frequency $\omega_n^a(s)$:[1,2,8,9]

$$[\mathbf{a}_n^g(s)]_\mu = \frac{D_{n\mu}(s)}{k_\mu^g(s)} \Big/ \sum_{\nu=1}^{N_{\text{vib}}} \frac{D_{n\nu}(s)^2}{k_\nu^g(s)} \tag{7}$$

$$k_n^a(s) = 1 \Big/ \sum_{\nu=1}^{N_{\text{vib}}} \frac{D_{n\nu}(s)^2}{k_\nu^g(s)} \tag{8}$$

$$m_n^a(s) = 1/G_{nn}(s) \tag{9}$$

$$\omega_n^a(s) = \sqrt{\frac{k_n^a(s)}{m_n^a(s)}} \tag{10}$$

where $D_{n\mu}(s)$ is an element of the **D**-matrix that connects normal coordinates with internal coordinates and $G_{nn}(s)$ is an element of the Wilson **G**-matrix.

For the decomposition of normal modes into AIMs, the amplitudes $A_{n,\mu}(s)$ are used:[1,2,8,9]

$$A_{n,\mu}(\mathbf{l},s) = \frac{[\mathbf{l}_\mu^\dagger(s)\mathbf{F}(s)\mathbf{a}_n(s)]^2}{[\mathbf{a}_n^\dagger(s)\mathbf{F}(s)\mathbf{a}_n(s)][\mathbf{l}_\mu^\dagger(s)\mathbf{F}(s)\mathbf{l}_\mu(s)]} \tag{11}$$

where **F**(s) denotes the force constant matrix calculated as a function of s.

7. Identification of vibrational modes that are converted into (generated from) translational or rotational modes. Vibrational frequencies that vanish during the reaction indicate modes that are converted into either rotations or translations of the RC. By decomposing these modes into AIMs it can be clarified which translation or rotation is generated. In the case of the carbene rearrangement (1), the total number of vibrational modes of the RC is preserved.

8. Analysis of the mode-mode coupling pattern. Calculation of the mode–mode coupling elements $B_{\mu,\nu}(s)$ given in Eqn. (12) provides an insight into energy dissipation.[1,2,5,35] If in an avoided crossing two vibrational eigenstates approach each other shortly (see step 5), they can exchange only little energy. The corresponding mode–mode coupling peak is relatively sharp and localized at a particular s-value. However, if the two vibrational eigenstates slowly approach each other and also slowly depart, thus staying together for a relatively large part Δs of the path, a larger amount of energy can be exchanged, leading to effective energy dissipation. The corresponding mode–mode coupling peak is relatively broad and delocalized over the area Δs:

$$B_{\mu,\nu}(s) = \tilde{\mathbf{l}}_\mu^g(s)^\dagger [\mathrm{d}\tilde{\mathbf{l}}_\nu^g(s)/\mathrm{d}s] = -B_{\nu,\mu}(s) \tag{12}$$

9. Presentation of the adiabatic force constants of the RC along the reaction path. The AIM force constants are given in Eqn. (8). They can be directly used to analyze changes in the electronic structure of the RC, in particular changes in bonding. Care has to be taken in those situations where the internal coordinate in question dominates the reaction path direction. Then, the adiabatic force constant becomes unusually large (often increasing to a maximum value) and reflects the coupling of the corresponding AIM and the motion along the reaction path.

10. Calculation of the reaction path curvature and the curvature coupling coefficients. Since the curvature of the reaction path is given by the vector $\mathbf{k}(s)$, it is more convenient to investigate the scalar curvature $k(s)$ given as the Euclidian norm of the curvature vector:

$$\kappa(s) = [\mathbf{k}(s)^\dagger \mathbf{k}(s)]^{1/2} = [\sum_{\mu=1}^{N_{\text{vib}}} B_{\mu,s}^2(s)]^{1/2} \tag{13}$$

where

$$\mathbf{k}(s) = \mathrm{d}^2\tilde{\mathbf{x}}(s)/\mathrm{d}s^2 \tag{14}$$

and

$$B_{\mu,s}(s) = \mathbf{k}(s)^\dagger \tilde{\mathbf{l}}_\mu^g(s) \tag{15}$$

are the curvature coupling coefficients. The latter describe the dynamic coupling between the translational motion along the reaction path and the $3K-7$ normal modes orthogonal to the reaction path. These couplings are important for mode selective rate enhancement experiments: A laser is tuned on the frequency of that normal mode that couples strongly with the motion along the path and energy is channeled in this way into the

reaction path maximally increasing the rate constant with a minimum of energy.[10,11]

11. Decomposition of the reaction path curvature in terms of adiabatic mode-curvature coupling coefficients:. The curvature vector can be analyzed in terms of AIMs utilizing amplitudes $A_{n,s}(\mathbf{k},s)$, which correspond to adiabatic curvature coupling coefficients:

$$A_{n,s}(\mathbf{k},s) = \frac{\mathbf{k}(s)^{\dagger}\mathbf{M}(s)\mathbf{a}_n^g(s)}{\sqrt{(\mathbf{a}_n^g)^{\dagger}(s)\mathbf{M}(s)\mathbf{a}_n^g(s)}} \tag{16}$$

Equation (16) indicates that the coefficients $A_{n,s}$ possess the same dimension as coefficients $B_{\mu,s}$ and become identical with the latter for $\mathbf{l}_\mu^g = \mathbf{a}_n^g$.[1]

12. Analysis of changes in the electron density distribution along the reaction path. This can be accomplished by calculating atomic charges, e.g. utilizing the NBO analysis[42] as done in this work. Alternatively, the electron density distribution, electron difference densities or the Laplacian of the electron density can be investigated for increasing s.[1,2,4]

13. Calculation of electric and magnetic properties of the RC along the reaction path. In this work, just the dipole moment μ was determined as a function of s. However, in principle it is possible to calculate a manifold of electric and magnetic properties along the path to monitor all changes in the electronic structure of the RC as detailed as possible.

14. Calculation of rate constants with the help of variational transition state theory (VTST). VTST was used in its canonical version (CVT).[43] Rate constants $k(1)$ were calculated in the range $T = 60$–500 K minimizing the flux of the trajectories of the RC through a dividing surface located in the TS region.

15. Investigation of quantum mechanical tunneling, isotope effects, etc. Tunneling corrections for the rate constants $k(1)$ obtained in step 14 were calculated with the CD-SCSAG method,[44] which can be applied if the curvature coupling elements related to the migrating H atom are not too large, which is true for reaction (1). The influence of tunneling was calculated for the temperature range 60–500 K.

Tunneling can be predicted from the curvature and the curvature coupling elements of Eqn. (15). The reaction path hamiltonian is given by

$$H(s,p_s,\{Q_\mu\},\{P_\mu\}) = T(s,p_s,\{Q_\mu\},\{P_\mu\}) + V(s,\{Q_\mu\}) \tag{17}$$

where the path parameter s and the normal coordinates $\{Q_\mu\}$ are the reaction valley coordinates and p_s and $\{P_\mu\}$ denote their conjugated momenta. The potential V is expressed in Eqn. (5) while the kinetic energy T takes the form

$$T(s,p_s,\{Q_\mu\},\{P_\mu\}) = \frac{1}{2}\left[p_s - \sum_{\mu,\nu}^{N_{\text{vib}}} B_{\mu,\nu}(s)Q_\mu(s)P_\nu(s)\right]^2 \Big/ \left[1 + \sum_{\mu}^{N_{\text{vib}}} B_{\mu,s}(s)Q_\mu(s)\right]^2 + \frac{1}{2}\sum_{\mu}^{N_{\text{vib}}} P_\mu^2(s) \tag{18}$$

The first term corresponds to the kinetic energy part of the movement along the path including the coupling terms between movement along the reaction path and transverse motions. The second term represents the kinetic energy part associated with a movement orthogonal to the path direction. The nominator of the first term is the generalized momentum of the motion along the path and the denominator represents an effective mass, which is of relevance for tunneling investigations. Curvature of the path lowers the effective mass [$B_{\mu,s}(s) < 0$] and, accordingly, raises the tunneling probability.[45–47]

The reaction valley was followed from the reactant to the product for reaction (1) ($-2.28 \leq s \geq 3.84$ amu$^{\frac{1}{2}}$) where the endpoints of the path correspond to structures within 0.1 kcal mol^{-1} of the energy of reactant and product, respectively. The RC possess C_1 symmetry, thus leading to 12 internal coordinates describing its geometry.

All calculations needed for URVA were carried out with the program ADIA, which is a multipurpose package for the analysis of vibrational spectra and carrying out URVA.[1,8,9] ADIA is a part of the *ab initio* package COLOGNE2000.[48] For the HF, MP2 and DFT calculations, the *ab initio* package Gaussian 98[49] was used. For VTST and the tunneling corrections a local version of the program POLYRATE[50] interfaced to COLOGNE2000 was used.

ANALYSIS OF REACTION PATH AND REACTION VALLEY

Calculated energies and geometries of the stationary points of reaction (1) are summarized in Table 1 and Fig. 1. Details of the reaction path and the reaction valley of reaction (1) are shown in Fig. 2 [energy profile $V(s)$], Fig. 3 [changes in the geometric parameters $q(s)$ of the RC], Fig. 4 [internal coordinate contributions to reaction path vector t(s)], Fig. 5 (internal forces of the RC), Figs 6 and 8 [vibrational frequencies $\omega_\mu^g(s)$ and mode–mode couplings $B_{\mu,\nu}(s)$], Fig. 7 (decomposition of normal mode 9 in

Table 1. Energetics of reaction (1): $H_3C—CCl \rightarrow H_2C{=}CHCl$[a]

Method/basis set	Molecule	$E/\Delta E$	$H/\Delta H$	$G/\Delta G$	S	μ
B3LYP/6–1G(d,p)	Carbene	−538.09773	−538.05277	−538.08440	67.0	2.29
	TS	13.7	11.7	12.8	63.0	3.29
	Vinyl chloride	−58.0	−56.6	−55.5	63.0	1.61
B3LYP/cc-pVTZ	Carbene	−538.16526	−538.12051	−538.15214	66.6	2.18
	TS	13.5	11.4	12.5	63.0	3.18
	Vinyl chloride	−57.5	−56.1	−55.0	63.0	1.48
CCSD(T)/cc-pVTZ	Carbene	−537.54363	−537.49888	−537.53051	66.6	
	TS	13.2	11.1	12.2	63.0	
	Vinyl chloride	−57.4	−56.0	−54.9	63.0	
Exp.[15]			4.3			

[a] Absolute energies (enthalpies) in hartree, relative energies (enthalpies) in kcal mol^{-1}, entropies in e.u., dipole moments μ in D. For the CCSD(T) calculations, B3LYP/cc-pVTZ geometries and vibrational corrections were used.

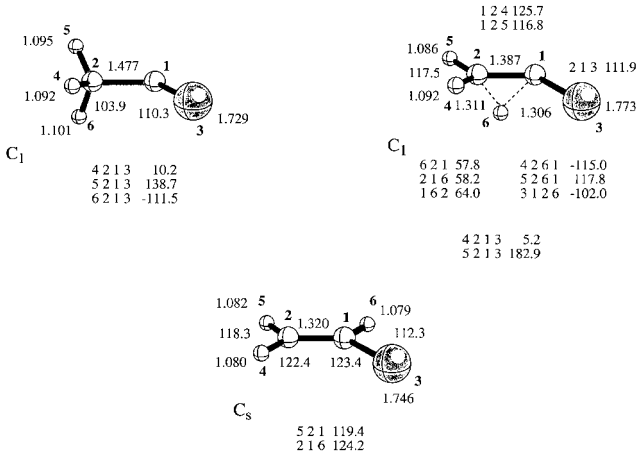

Figure 1. B3LYP/cc-pVTZ geometries of reactant, TS and product of reaction (1). Distances in Å, angles in degrees

terms of AIMs), Figs 9 and 10 (reaction path curvature and its decompositions into normal modes and into AIMs) and Fig. 11 (adiabatic force constants). The analysis along the reaction path is based on Figs 2–5 and that of the $(3K-7)$-dimensional orthogonal vibrational space on Figs 6–11.

In these figures, in which a given property of the RC is represented as a function of the s, the position of the TS is defined by a dashed vertical line at $s = 0$, i.e. the reactant (chlorocarbene) is located at $s = -2.28$ $amu^{\frac{1}{2}}$ bohr and the product (vinyl chloride) at $s = +3.84$ $amu^{\frac{1}{2}}$ bohr. Actually, the calculation was stopped at an energy 0.04 kcal mol^{-1} above the reactant and 0.008 kcal mol^{-1} above the product. Investigation of the frequencies and couplings, however, revealed that the calculation of the reaction valley becomes unstable at $s = -1.9$ and

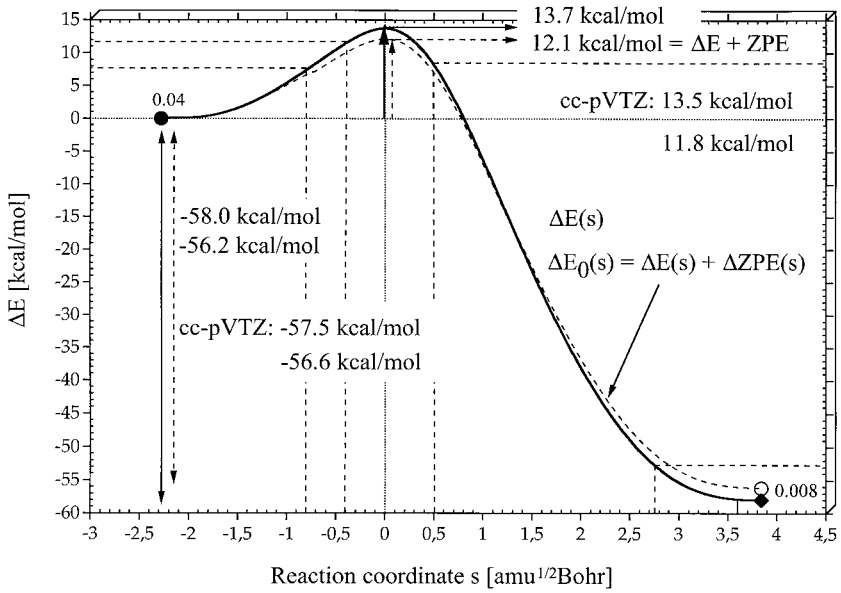

Figure 2. B3LYP/6–31G (d,p) energies V (solid line) and $V + ZPE$ (dashed line) as a function of the reaction path coordinate s for the reaction (1). The position of the TS corresponds to $s = 0$ $amu^{1/2}$ Bohr. Results obtained at other levels of theory are also given. The energy separation from the reactant and the product is given at the starting and terminating point of the reaction path in kcal/mol

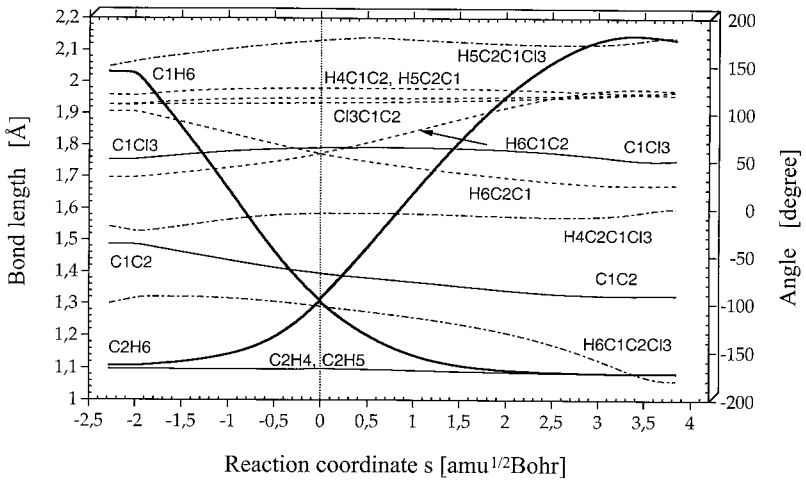

Figure 3. B3LYP/6–31G(d,p) geometrical parameters q of the reaction complex RC of reaction (1) given as a function of the reaction coordinate s. For the numbering of atoms, see Fig. 1. The position of the TS corresponds to s = 0 amu$^{\frac{1}{2}}$ bohr and is indicated by a dashed vertical line

$s = 3.7$ amu$^{\frac{1}{2}}$ bohr, although the accuracy of energy and gradient still seem to be reasonable. At these points the reaction valley is already very flat and an exact determination of the curvature of the reaction valley becomes more difficult.

Analysis of the reaction path

Reaction (1) is exothermic by 57.5 kcal mol^{-1} and possesses an activation energy of 13.5 kcal mol^{-1} (B3LYP/cc-pVTZ results, Table 1). The corresponding activation enthalpy is 11.4 kcal mol^{-1}, which differs only slightly from the CCSD(T) result (Table 1), the MP4 value reported by Storer and Houk[17] or the DFT values reported by Houk and co-workers.[18] Energies and enthalpy differences obtained with the 6–31G(d,p) basis set are marginally larger (0.2–0.3 kcal mol^{-1}, Table 1, Fig. 1) so that we can conclude that B3LYP with a VDZP basis set provides already a reliable account of the energetics of reaction (1) and, by this, also of reaction path and reaction valley. The results obtained in this work

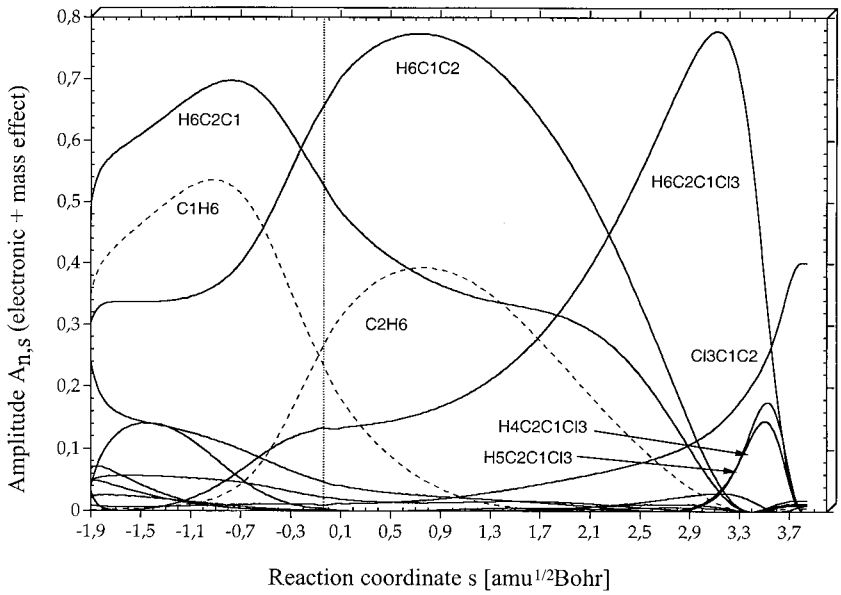

Figure 4. Characterization of the reaction path vector $\mathbf{t}(s)$ of reaction (1) in terms of internal coordinate modes using amplitudes $A_{n,s}$ considering electronic and mass effects according to Eqn. ((10)). The position of the TS corresponds to s = 0 amu$^{\frac{1}{2}}$ bohr and is indicated by a dashed vertical line. B3LYP/6–31G(d,p) calculations

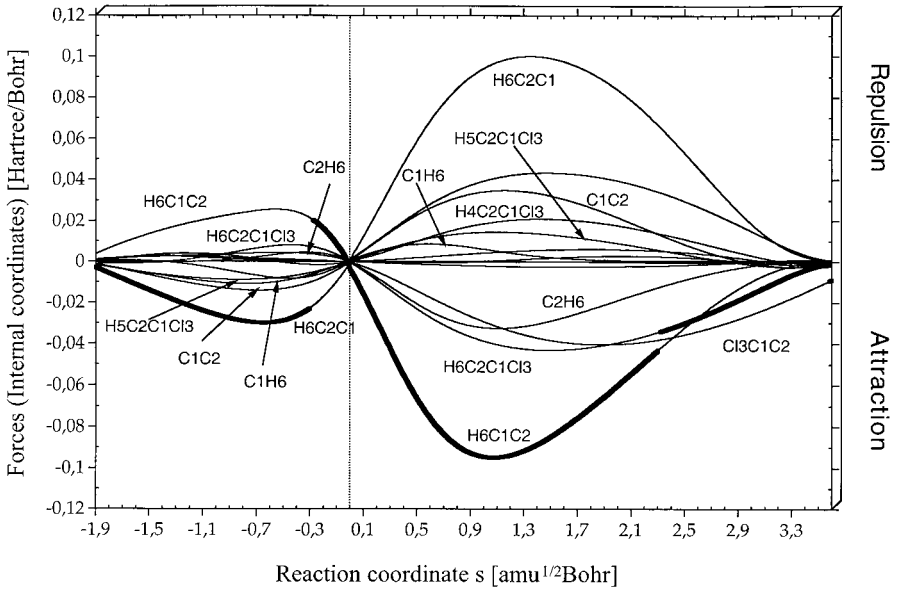

Figure 5. Decomposition of the gradient along the path of reaction (1) in terms of attractive or repulsive internal forces. The position of the TS corresponds to s = 0 amu$^{\frac{1}{2}}$ bohr and is indicated by a dashed vertical line. Internal forces associated with the internal coordinates that dominate the direction of the reaction path (compare with Fig. 4) are given in bold. B3LYP/6–31G(d,p) calculations

and those by Houk and co-workers[17,18] clearly indicate that the activation enthalpy of reaction (1) in the gas phase is 2.6 times larger than the measured value corresponding to the solution phase. Also, the calculated activation entropy ($\Delta S\ddagger = -3.6$ .u, Table 1) is far from indicating a highly ordered TS as is suggested by the measured *A* factor.[14] Hence reaction (1) has a much lower activation enthalpy in heptane solution (4.3 kcal mol^{-1}) because of specific or non-specific solvation.[14]

Changes in the geometry of the reaction complex. Figure 3 indicates that the changes in distances C2H6 (breaking bond) and C1H6 (forming bond) are related. The smaller is the distance C2H6, the larger is the

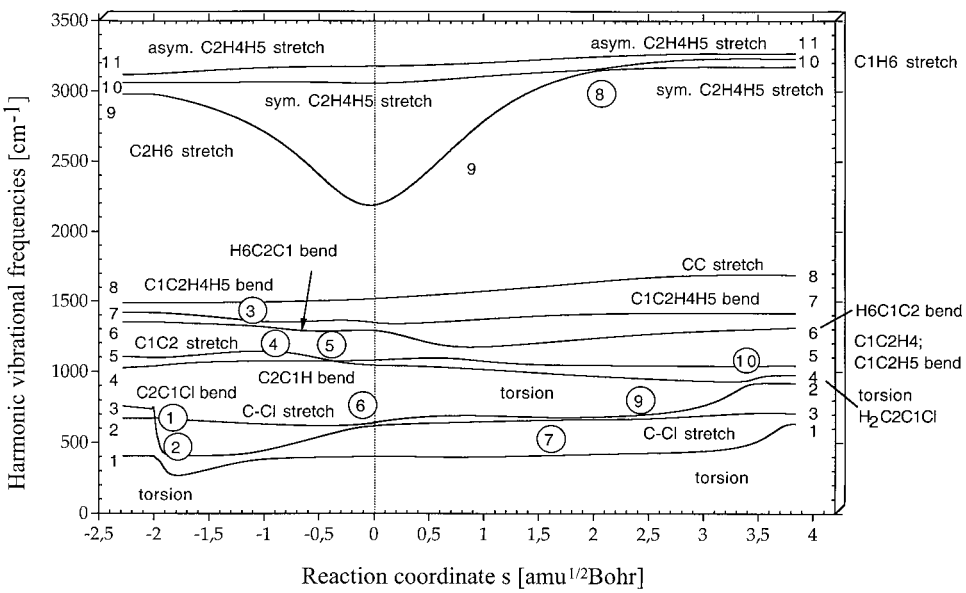

Figure 6. Representation of normal mode frequencies $\omega_\mu(s)$ of the RC of reaction (1) as a function of the reaction path length *s*. The numbering of normal modes is given according to the order of normal modes calculated for the reactant. All modes are characterized on the basis of an AIM analysis. Encircled numbers indicate positions of mode-mode coupling (compare with Fig. 8). The position of the TS corresponds to s = 0 amu$^{\frac{1}{2}}$ bohr and is given by a dashed vertical line. B3LYP/6–31G(d,p) calculations

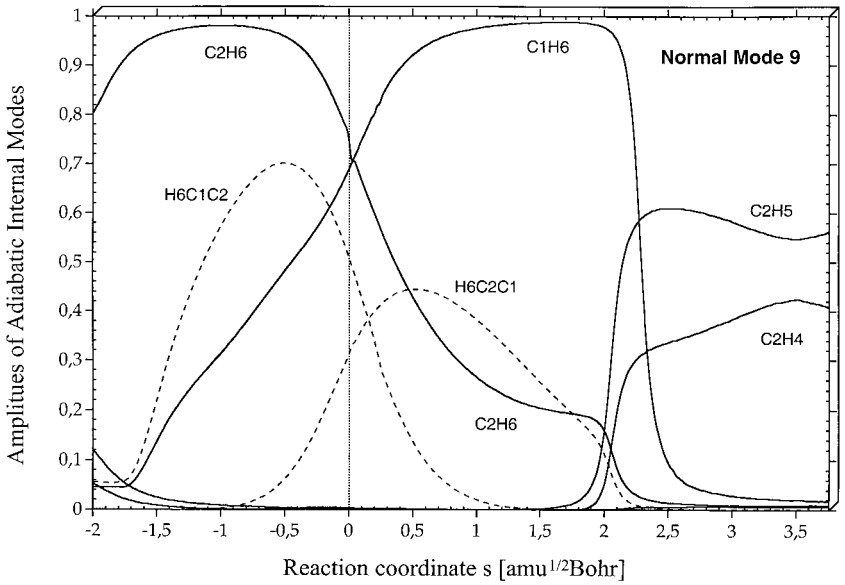

Figure 7. Characterization of mode 9 of the RC of the reaction (1) in terms of generalized adiabatic internal modes (AIMs). The position of the transition state corresponds to s = 0 amu$^{\frac{1}{2}}$ bohr and is indicated by a dashed vertical line. B3LYP/6–31G(d,p) calculations

distance C1H6 (entrance channel) and vice versa (exit channel). The two distances are equal at $s = 0$ amu$^{\frac{1}{2}}$ bohr (Fig. 3), i.e. at the TS the migrating H atom adopts a central position over the bond C1C2 (C2H6, 1.311; C1H6, 1.306 Å; angle C6C2C1, 57.8; C2C1C6, 58.2°; Fig. 1). Closer inspection of Fig. 3 reveals, however, that changes in C2H6 and C1H6 are either slowed relative to those of the other parameters (C2H6 in the range $-2 < s < -0.5$ amu$^{\frac{1}{2}}$ bohr; C1H6 in the range $0.5 < s < 2$ amu$^{\frac{1}{2}}$ bohr; Fig. 3). Hence the breaking and forming of the CH bonds, although occurring simultaneously, do not seem to be fully

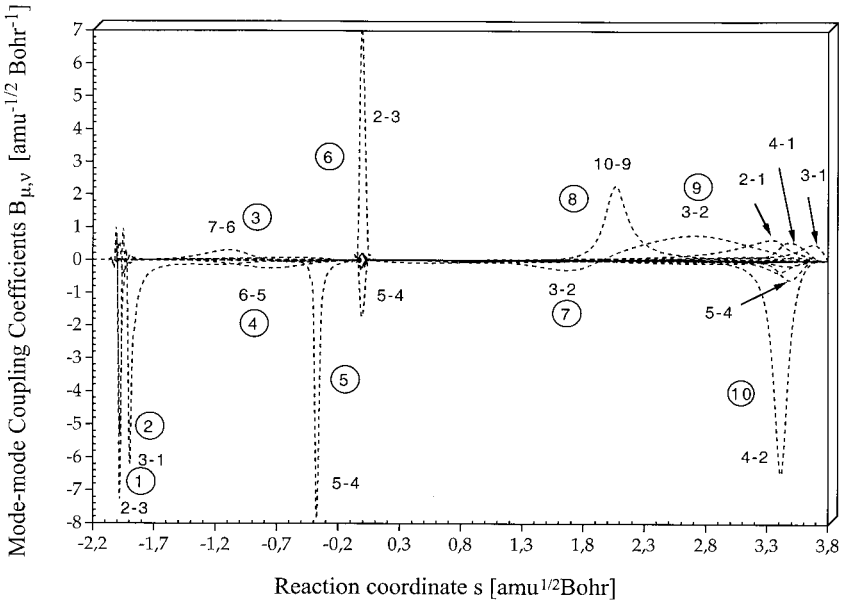

Figure 8. Mode–mode coupling coefficients $B_{\mu,\nu}$ given as a function of the path length s of reaction (1). All 55 mode combinations are considered and the $B_{\mu,\nu}(s)$ peaks are identified by appropriate normal mode labels (compare with Fig. 6) and numbered from the entrance to the exit channel (encircled numbers). Sharp peaks of $B_{\mu,\nu}(s)$ indicate diabatic energy exchange while broad peaks suggest energy dissipation between the corresponding modes. The position of the TS corresponds to s = 0 amu$^{\frac{1}{2}}$ bohr and is given by a dashed vertical line. B3LYP/6–31G(d,p) calculations

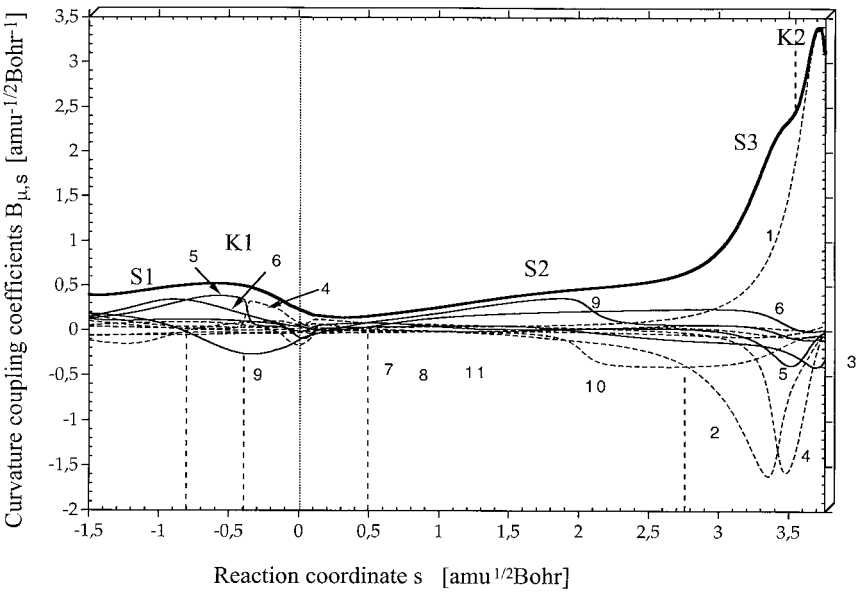

Figure 9. Decomposition of the scalar reaction path curvature $\kappa(s)$ (thick solid line) for reaction (1) in terms of normal mode-curvature coupling coefficients $B_{\mu,s}(s)$ (thin or dashed lines) where the most important modes μ are indicated. Curvature peaks are numbered *K*1 and *K*2, curvature shoulders as *S*1 and *S*2. The position of the TS corresponds to s = 0 amu$^{\frac{1}{2}}$ bohr and is indicated by a dashed vertical line. B3LYP/6–31G(d,p) calculations

synchronized. It is also obvious that the C1C2 bond does not increase linearly with increasing *s* and that the bond length C1Cl increases (up to $s = 2.5$ amu$^{\frac{1}{2}}$ bohr, Fig. 3) before it becomes shorter again, i.e. the C1Cl bond is not simply a spectator bond such as C2H4 or C2H5 but indirectly participates in the electronic structure changes along the reaction path. Also, the changes in all bond and dihedral angles (in particular H4C2C1Cl, H5C2C1Cl and H6C2C1Cl, which turn out to lead to strongly curved $q_n(s)$ functions when enlarging Fig. 3) suggest that the

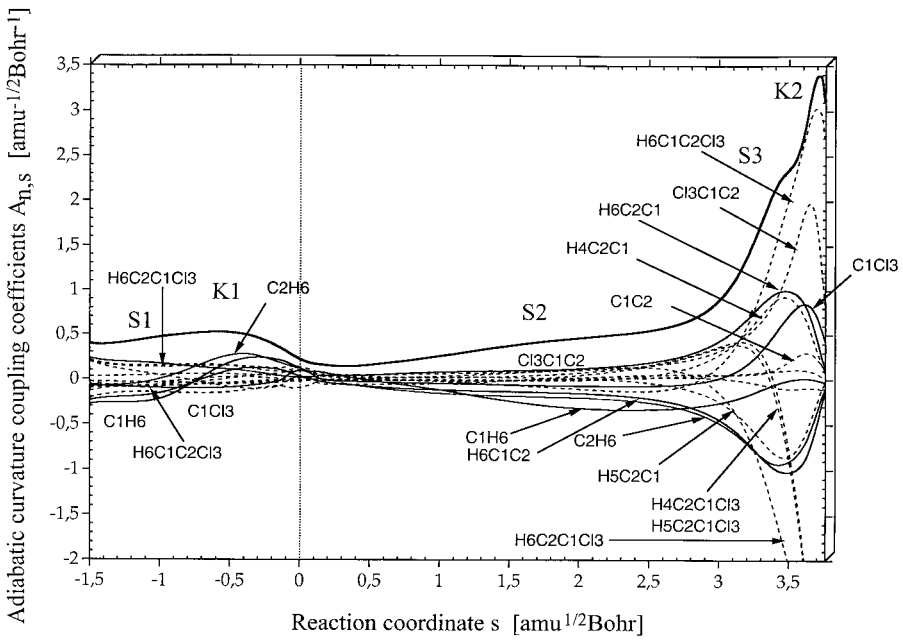

Figure 10. Decomposition of the scalar reaction path curvature $\kappa(s)$ (thick solid line) of reaction (1) in terms of adiabatic mode-curvature coupling amplitudes $A_{n,s}(s)$ (dashed lines). A redundant coordinate set was used for the analysis (see text). Curvature peaks (shoulders) and reaction regions are indicated. The position of the TS corresponds to s = 0 amu$^{\frac{1}{2}}$ bohr and is indicated by a dashed vertical line. B3LYP/6–31G(d,p) calculations

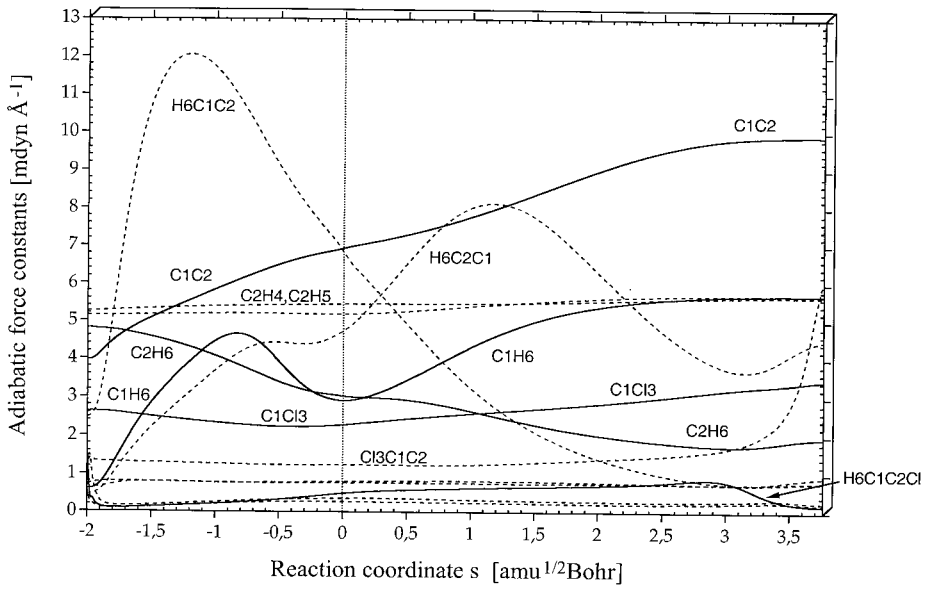

Figure 11. Generalized adiabatic force constants associated with the internal parameters described in Scheme 1. The position of the TS corresponds to s = 0 amu$^{\frac{1}{2}}$ bohr and is indicated by a dashed vertical line. B3LYP/6–31G(d,p) calculations

reaction mechanism involves significant changes in nearly all internal coordinates and is more complicated than just the simultaneous breaking and forming of a CH bond.

Reaction path direction. Decomposition of the reaction path vector $\mathbf{t}(s)$ (Fig. 4) reveals that a description of the migrating atom H6 in terms of angles H6C2C1 (entrance channel) and H6C1C2 (exit channel) is equivalent and preferable (stronger dominance in the reaction path direction) than a description in terms of distances C1H6 and C2H6. Both are given in Fig. 4, which is based on a redundant set of internal coordinates. It is also interesting that at $s = 2.3$ amu$^{\frac{1}{2}}$ bohr the dihedral angle H6C1C2Cl takes over to dominate the direction path direction and even a fourth internal coordinate, the angle ClC1C2 becomes important closely before reaching the product. This suggests that three, if not four, different stages can be distinguished along the reaction path. Tentatively, we associate these stages with the chemical processes of C2H6 bond breaking, C1H6 bond forming (both occurring simultaneously) and planarization at C2, which finishes the formation of the CC double bond. This seems to be in line with the simplified mechanism presented in Scheme 1(b).

Internal forces. The large forces exerted on the atoms of the RC (Fig. 5) are those connected with the bending of the angles H6C2C1 and H6C1C2, i.e. those internal coordinates which determine the direction of the reaction path up to $s = 2.2$ amu$^{\frac{1}{2}}$ bohr. The force H6C2C1 dominating in the entrance channel of reaction (1) is attractive until at $s = -0.4$ amu$^{\frac{1}{2}}$ bohr where the repulsive force H6C1C2 takes over. Up to $s = -0.4$ amu$^{\frac{1}{2}}$ bohr, there are just small changes in the distance C2H6 (Fig. 3) and a reduction of the bond angle H6C2C1 increases the hyperconjugative delocalization of the C2H6 bonding electron pair into the empty pπ orbital at the carbene atom C1 [see Scheme 1(b)]. Beyond this point the distance C2H6 increases linearly with the path length s (Fig. 3), which leads to the dominance of the repulsive force C2H6 or equivalently the repulsive force H6C1C2.

Once the TS is passed, the migrating atom H6 is closer to C1 than C2 and therefore attracted to C1, which is equivalent to an opening of the angle H6C1C2. At $s = 2$ amu$^{\frac{1}{2}}$ bohr the dihedral H6C1C2Cl, which describes the movement of H6 into the heavy atom plane and, by this, planarization at C1, takes over associated with an attractive, decreasing force.

The dominating forces exerted on the atoms of the RC are mostly attractive along the reaction path. This is in line with the mechanistic model that hyperconjugative delocalization already present in the reactant is just enhanced in the first part of the reaction (up to -0.4 amu$^{\frac{1}{2}}$ bohr) and that once a small barrier has been surmounted almost 70 kcal mol^{-1} are set free in the reaction. The three chemical process (C2H6 bond cleavage, C1H6 bond formation and C1C2 double bond formation) take place simultaneously, but bond cleavage is much faster accomplished than the slow formation of the new bonds.

The calculated NBO charges reveal that negative charge at C2 is decreased along the reaction path while it is increased at C1. This is in line with the model that H6 carries a significant part of the C2H6 bonding electron pair towards C1. The dipole moment of

methylchlorocarbene (2.29 D, Table 1) increases toward the TS (3.29 D) before it decreases again to the value adopted in vinyl chloride (1.61 D). At the TS, stabilizing electrostatic interactions with a solvent will be large so that a reduction of the energy barrier in solution can be expected.

Analysis of the reaction valley

The investigation of the $(3K-7)$ dimensional vibrational space is important for an understanding of the reaction mechanism, in particular for the description of energy transfer and energy dissipation.

Normal mode frequencies. The valley of reaction (1) is spanned by the normal coordinates of 11 vibrational modes, five of which are bond stretching modes, four (exit channel: 3) are bending modes, and one (3) is a torsional mode (Fig. 6). Mode 9 (see Fig. 7) corresponds in the entrance channel to the C2H6 stretching mode, its frequency is reduced by almost 800 cm^{-1} at the TS; in the exit channel it converts to the C1H6 stretching mode and crosses at 2 $amu^{\frac{1}{2}}$ bohr with mode 10 (mode–mode coupling 8, Fig. 6) to exchange its character with the latter, which corresponds to the symmetric H4C2H5 stretching mode. The decomposition of mode 9 into AIMs is shown in Fig. 7. The characterization of the other normal modes was carried out in the same way (not shown here) and is the basis for the analysis of mode–mode couplings and curvature couplings.

Mode-mode coupling. Mode–mode coupling coefficients $B_{\mu\nu}(s)$ are shown in Fig. 8 where each coupling peak is identified by an encircled number (compare with Fig. 6) and the modes μ and ν involved in the coupling. At the positions of the sharp $B_{\mu\nu}(s)$ peaks localized diabatic transitions between two modes take place so that both the character and the energy carried by the first mode is transferred to the second mode. Delocalized couplings leading to broad peaks are characterized by a distribution of the energy carried by one mode over both modes so that energy dissipation can occur. In this way, Fig. 8 provides information about energy transfer and the degree of energy dissipation between the vibrational modes.

Energy dissipation takes place in the exit channel, in particular between the CH stretching modes (8, modes 10–9) thus distributing the energy set free from the formation of the bond C1H6 and between the torsional modes and the C–Cl stretching mode (10, 4–2; 9, 3–2). In the entrance channel and at the TS energy can be exchanged between various low-frequency modes (1, 2–3; 2, 3–1; 5, 5–4; 6, 2–3; Fig. 8), however none of the couplings involves mode 9, i.e. if energy is pumped into 9 (the C2H6 stretching mode), energy will not be lost by exchange/distribution with other vibrational modes. However, pumping of energy into the C1C2 stretching mode (mode 5, Fig. 6) would be largely lost into the bending mode 4 and, therefore, would not help to accelerate the reaction.

Reaction path curvature. The reaction path curvature $\kappa(s)$ (Fig. 9) of reaction (1) is characterized by a shoulder $S1$ (-2.28 to -0.8 $amu^{\frac{1}{2}}$ bohr) and a small curvature peak $K1$ in the entrance channel at $s = -0.4$ $amu^{\frac{1}{2}}$ bohr, a long shoulder $S2$ between 0.5 and 2.75 $amu^{\frac{1}{2}}$ bohr, another shoulder $S3$ between 2.75 and 3.5 $amu^{\frac{1}{2}}$ bohr and a relatively large curvature peak $K2$ at 3.65 $amu^{\frac{1}{2}}$ bohr. The curvature couplings responsible for $S1$ involve normal mode 6, those for $K1$ modes 5, 4 and 9, those for $S2$ modes 9 and 10, those for $S3$ modes 2, 4 and 1 and those for $K2$ modes 4 and 1 where smaller contributions are not listed (Fig. 9). In view of the low reaction path curvature in the entrance channel, there is little chance of enhancing the rate of the 1,2-H shift by pumping energy into the C2H6 stretching mode 9.

The decomposition of the scalar curvature in terms of adiabatic curvature couplings (Fig. 10) provides a basis to associate curvature peaks and shoulders with the internal coordinates of the RC, which in turn describe the chemical processes taking place. (The same result is achieved if the normal mode contributions to the curvature are decomposed into AIM contributions as in Fig. 7. The latter approach was used because, with an increasing number of small contributions, it is difficult to find the most significant ones in Fig. 10.)

Curvature shoulder $S1$ and peak $K1$ result from a bending of the angle H6C2C1 (mode 6), rehybridization at C2 and, by this, a change in the bond length C1C2 (mode 5), followed by a slight upward movement of H4 into the heavy atom plane (mode 4). Changes in the CC bond length and the position of H4 are overlayed by a lengthening of C2H6 (mode 9), which represents the largest curvature coupling contribution to $K1$. Hence, preparation for C2H6 bond breaking takes place in the range from s = -2.28 to -0.8 $amu^{\frac{1}{2}}$ bohr while the bond breaking process occurs between -0.8 and 0 $amu^{\frac{1}{2}}$ bohr with the maximum at -0.4 $amu^{\frac{1}{2}}$ bohr.

The shoulder $S2$ is predominantly due to the curvature couplings involving the shortening of the new C1H6 bond, which is essentially finished at 2.75 $amu^{\frac{1}{2}}$ bohr. At this point, the newly formed vinyl chloride is still pyramidalized both at C1 (H6C1C2H, 22°; ClC1C2H, 8°) while it is largely planar at C2 (see Fig. 1, TS geometry). Planarization at C1 finalizes the double bond formation of the product, which takes place in the range of curvature peak $K2$ [inclusive shoulder $S3$ (Fig. 10)].

Adiabatic force constants. The reaction mechanism as it develops from the investigation of the reaction path direction, the forces exerted on the RC and the curvature coupling coefficients is confirmed by the calculated adiabatic force constants (Fig. 11). The AIM force

constants for bond stretching and angle bending are large enough that their changes along the reaction path can be easily followed. The stretching force constants of spectator bonds (C2H4, C2H5) do not change significantly. Strong changes of the stretching force constants of C2H6, C1H6 and C1C2 make it possible to identify the various stages of the reaction mechanism. The C1Cl bond might also be considered as a spectator bond; however, its stretching force constant changes significantly and suggests that the strength of the CCl bond reflects the position of the migrating H atom.

Strongly exaggerated force constants (reaching a maximum before they decrease again) indicate a coupling of the corresponding AIM with the reaction path. As already discussed in connection with the reaction path direction, angle parameters are in this connection more sensitive than the CH bond parameters and, therefore, they can be used to represent changes in the force constants of the latter: H6C1C2 for C2H6 and H6C2C1 for C1H6 [we note that for the geometric description of the RC angle, H6C2C1 is important in the entrance channel whereas for its energetic description bending force constant H6C1C2 (corresponding to the stretching force constant C2H6) has to be used]. Before the TS, the translational mode couples with the C2H6 stretching motion (as reflected by the bending force constant H6C1C2), and after the TS, it couples with the C1H6 stretching motion (as reflected by the bending force constant H6C2C1). At the TS, the C2H6 cleaving and the C1H6 forming bond have about the same strength according to the corresponding AIM stretching force constants. The formation of the C1H6 bond is finished at about 2.75 $\text{amu}^{\frac{1}{2}}$ bohr where it reaches the strength of the spectator bonds C2H4 and C2H5. At this stage the C1C2 double bond has not gained its full strength. This is accomplished by planarization at C1 as reflected by the coupling of the C2C1Cl AIM with the reaction path motion (maximum of the corresponding AIM force constant; see also changes in the torsional force constant H6C1C2Cl; Fig. 11).

DISCUSSION OF THE REACTION MECHANISM AND CHEMICAL RELEVANCE OF RESULTS

Using the results of the analysis of reaction path and reaction valley the following mechanistic steps can be distinguished for reaction (1):

1. Preparation of the reactant (shoulder *S*1, $-2.28 < s < -0.8$ $\text{amu}^{\frac{1}{2}}$ bohr): H6C2C1 bending initiates a rehybridization at the C2 atom.
2. TS region (region of curvature peaks *K*1 and shoulder *S*2, $-0.8 < s < 2.75$ $\text{amu}^{\frac{1}{2}}$ bohr; Fig. 11): in this range the bond C2H6 is broken and the bond C1H6 simultaneously formed where, however, the latter process takes considerably more time than the former process. Parallel to this the C1C2 double bond is formed.
3. Preparation of the product (region of curvature shoulder *S*3 and peak *K*2, $2.75 < s < 3.8$ $\text{amu}^{\frac{1}{2}}$ bohr; Fig. 11): in the range of shoulder *S*3 and peak *K*2, the formation of the double bond is finished as a result of planarization and associated rehybridization at atom C1.

The center of the transition state region is at 0.97 $\text{amu}^{\frac{1}{2}}$ bohr, which means that the energy TS is shifted by 0.97 $\text{amu}^{\frac{1}{2}}$ bohr into the entrance channel typical of a strongly exothermic reaction. According to orbital symmetry rules, the 1,2-H shift reaction (1) is symmetry-allowed. As found previously for symmetry-allowed reactions, changes in the geometrical parameters occur simultaneously, in a concerted manner, so that the energy increase along the reaction path toward the TS is minimized. Curvature and curvature couplings of these reactions seem to be in general small, contrary to those observed for symmetry-forbidden reactions.[4]

Since the reaction is a consequence of hyperconjugative delocalization of the C2H6 bonding electron pair into the empty pπ orbital at C1, only a relatively small energy increase (ca 7.5 kcal mol^{-1}; Fig. 2) is needed to prepare for the 1,2-H shift and just another 6 kcal mol^{-1} are needed to reach the energy TS (Fig. 2). The low barrier is clearly a consequence of the fact that the energy needed for the breaking of the C2H6 bond is largely compensated by the increasing strength of the C1C2 and C1H6 bonds.

This is the first case where changes of the curvature in the preparation region are larger than those in the TS region and that a conformational change (planarization at C1) is indicated by a relatively strong curvature peak while the actual chemical processes of bond breaking and bond formation do not lead to significant changes in the curvature (just small peaks or shoulders). Accordingly, the curvature couplings associated with the chemical processes (mode 9, C2H6 bond breaking and C1H6 bond formation) are also relatively small. We can predict from these couplings that H tunneling will accompany the reaction; however, it will not be particularly large and can not be solely responsible for the observed curvature in the Arrhenius plots.

In Table 2, calculated kinetic parameters are summarized. At room temperature, the CVT rate constant [without tunneling corrections: $k(1) = 3.03 \times 10^3$ s^{-1}; Table 2] is a factor of 1000 smaller than the measured rate constant, which is not surprising in view of the large discrepancy between the calculated and measured activation enthalpies: 11.4 vs 4.3 kcal mol^{-1}. Quantum mechanical tunneling increases the rate constant by a factor of 9 to 2.74×10^4 s^{-1} (Table 2). This implies an effective activation enthalpy at 300 K of 7.4 kcal mol^{-1}, which is still 3 kcal mol^{-1} larger than the measured activation enthalpy (corresponding to a factor of 100 in the ratio of calculated and measured rate constant; Table

Table 2. CD-SCSAG tunneling transmission factors χ, CVT reaction rates k_{CVT} and CD-SCSAG tunneling-corrected CVT reaction rates $k_{CD-SCSAG}$ for reaction (1): $H_3C—CCl \rightarrow H_2C = CHCl$[a]

Method/basis set	Temperature	χ	k_{CVT}	$k_{CD-SCSAG}$
B3LYP/6–31G(d,p)	60	1.58×10^{33}	6.21×10^{-33}	9.80
	70	8.34×10^{26}	1.43×10^{-26}	1.19×10^{1}
	80	1.68×10^{22}	8.15×10^{-22}	1.43×10^{1}
	100	4.92×10^{15}	4.14×10^{-15}	2.03×10^{1}
	200	2.34×10^{3}	1.01×10^{-1}	2.37×10^{2}
	300	9.04	3.03×10^{3}	2.74×10^{4}
Exp.[15]	203 to 353	In heptane		1.36×10^{6}

[a] Temperatures in K and reaction rates in s^{-1}.

2). Contrary to Storer and Houk,[17] we suggest that the mechanism of reaction (1) in the gas phase is different from that in solution. H tunneling, although significant to determine the rate constant accurately, cannot explain the strong non-linearity in measured Arrhenius correlations (see Fig. 12, where the temperature range of measurements is indicated).

Specific interactions between chlorocarbene and a solvent molecule, e.g. in form of electrostatic attraction between the partially negatively charged Cl atom and a partially positively charged H atom of the solvent molecule heptane as indicated in Scheme 1(c), can increase the effective electronegativity of Cl, which will result in a lowering of the energy of the empty pπ orbital of C1. Hyperconjugative interactions between C1H6 and the empty pπ orbital will be increased, thus reducing the barrier. In view of the relatively large dipole moment (3.3 D; Table 1) calculated for the TS (also Cl carries a negative charge in the TS but not in the reactant), non-specific solvation will play an increasing role in stabilizing the TS when the dielectric constant of the solvent becomes larger. It has been argued that bimolecular reactions or the generation mode of the carbene rather than H tunneling are responsible for the observed non-linearity of the Arrhenius correlations found for reaction (1).[14] Our calculations show that this is essentially correct, although H tunneling cannot be neglected for the gas-phase reaction while its role should became small in the case that solvent effects lower the energy barrier, which was verified experimentaly for reaction (2).[23]

We conclude that intramolecular rearrangements such

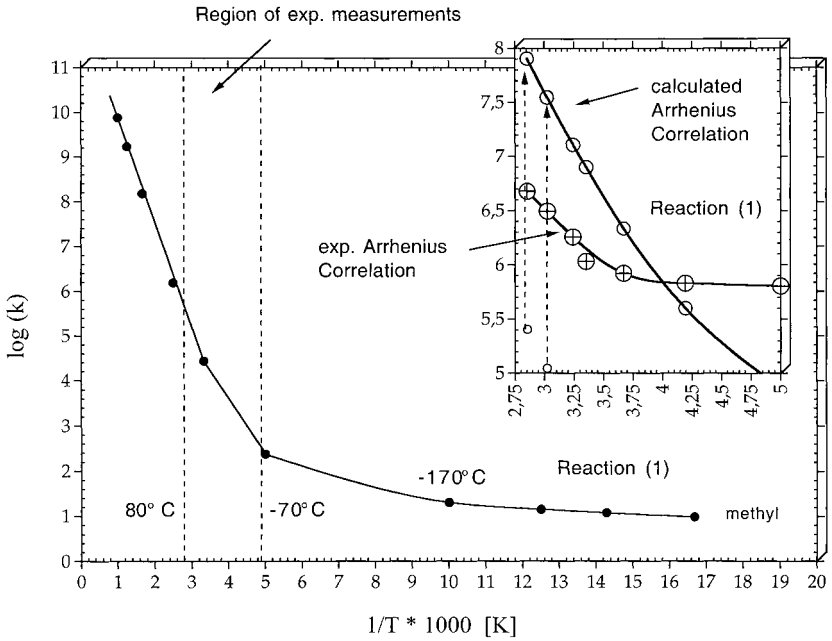

Figure 12. Calculated and measured Arrhenius correlations for reaction (1) (compare with Table 2). The temperature range of measurements is indicated. In the inset, the measured and the calculated Arrhenius correlation for reaction (1) are compared where in the latter case calculated log *k* values (see circles in the lower left corner of the inset) are shifted upwards by +2.5 to fit into the range of measured log *k* values. B3LYP/6–31G(d,p) calculations

as 1,2-H shifts in carbenes (or similarly in carbocations), which are initiated by hyperconjugative interactions are characterized by energy barriers that result to a larger part from conformational changes preparing for the reaction rather than the chemical processes (CH bond cleavage/formation, CC double bond formation). Accordingly, the largest curvature peaks of the curvature diagram are due to the conformational changes while the chemical processes are just represented by small curvature peaks or shoulders. H tunneling plays a role as long as the energy barrier is not reduced by substituent or solvent stabilization of the TS. This explains why in the polar 1,1,2,2-tetrachloroethane a linear Arrhenius correlation was found for reaction (2).[23] In the temperature range of experimental measurements (−70 to 80 °C) the calculated Arrhenius correlation based on tunneling corrected reaction rates is weakly non-linear for reaction (1) (Fig. 12) and cannot explain the experimental observation of a strongly curved Arrhenius correlation. This supports explanations that associate non-linearity of the Arrhenius correlation with bimolecular reactions of the carbene.[14] Work is in progress to verify these explanations by quantum chemical calculations.

Acknowledgements

This work was supported by the Swedish Natural Science Research Council (NFR). All calculations were done on the supercomputers of the Nationellt Superdatorcentrum (NSC), Linköping, Sweden. The authors thank the NSC for generous allotment of computer time.

REFERENCES

1. Konkoli Z, Kraka E, Cremer D. *J. Phys. Chem. A* 1997; **112**: 1742.
2. Kraka E. In *Encyclopedia of Computational Chemistry*, vol. 4, Schleyer PvR, Allinger NL, Clark T, Gasteiger J, Kollman PA, Schaefer HF III, Schreiner PR (eds). Wiley: Chichester, 1998; 2437.
3. Konkoli Z, Cremer D, Kraka E. *J. Comput. Chem.* 1997; **18**: 1282.
4. Cremer D, Wu A, Kraka E. *Phys. Chem. Chem. Phys.* 2001; **3**: 674.
5. Miller WH, Handy NC, Adams JE *J. Phys. Chem. A* 1980; **72**: 99.
6. Fukui K. *J. Phys. Chem.* 1970; **74**: 4161.
7. Fukui K. *Acc. Chem. Res.* 1981; **14**: 363.
8. (a) Konkoli Z, Cremer D. *Int. J. Quantum Chem.* 1998; **67**: 1; (b) Konkoli Z, Larsson LA, Cremer D. *Int. J. Quantum Chem.* 1998; **67**: 11; (c) Konkoli Z, Larsson LA, Cremer D. *Int. J. Quantum Chem.* 1998; **67**: 29.
9. Cremer D, Larsson LA, Kraka E. In *Theoretical and Computational Chemistry*, Vol. 5, *Theoretical Organic Chemistry*, Párkányi C (ed). Elsevier: Amsterdam, 1998; 259.
10. (a) Morokuma K, Kato S. In *Potential Energy Characteristics for Chemical Reactions*, Truhlar DG (ed). Plenum Press: New York, 1981; 243; (b) Miller WH. In *The Theory of Chemical Reaction Dynamics*, Clary CD (ed). Reidel: Dordrecht, 1986; 27; (c) Truhlar DG, Garrett B. *Annu. Rev. Phys. Chem.* 1986; **35**: 159; (d) Truhlar DG, Steckler R, Gordon M. *Chem. Rev.* 1987; **87**: 217; (e) Truhlar DG, Brown F, Steckler R, Isaacson AD. In *The Theory of Chemical Reaction Dynamics*, Clary CD (ed). Reidel: Dordrecht, 1986; 285.
11. Kraka E, Dunning TH Jr. In *Advances in Molecular Electronic Structure Theory: the Calculation and Characterization of Molecular Potential Energy Surfaces*, Dunning TH Jr (ed). JAI Press: Greenwich, CT, 1990; 129.
12. (a) Gray SK, Miller WH. *J. Chem. Phys.* 1980; **73**: 2733; (b) Carrington T Jr, Miller WH. *J. Chem. Phys.* 1984; **81**: 3942.
13. Colwell SM, Handy NC. *J. Chem. Phys.* 1985; **82**: 1281.
14. La Villa JA, Goodman JL. *J. Am. Chem. Soc.* 1989; **111**: 6877.
15. Dix EJ, Herman MS, Goodman JL. *J. Am. Chem. Soc.* 1993; **115**: 10424.
16. La Villa JA, Goodman JL. *Tetrahedron Lett.* 1990; **31**: 5109.
17. Storer JW, Houk KN. *J. Am. Chem. Soc.* 1993; **115**: 10426.
18. Keating AE, Garcia-Caribay MA, Houk KN. *J. Am. Chem. Soc.* 1998; **102**: 8467.
19. Liu MTH, Bonneau R. *J. Am. Chem. Soc.* 1990; **112**: 3915.
20. Liu MTH, Bonneau R. *J. Am. Chem. Soc.* 1992; **114**: 3604.
21. Liu MTH. *Acc. Chem. Res.* 1994; **27**: 289.
22. Liu MTH, Bonneau R, Wierlacher S, Sander W. *J. Photochem. Photobiol. A: Chem.* 1994; **84**: 133.
23. Merrer DC, Moss RA, Liu MTH, Banks JT, Ingold KU. *J. Org. Chem.* 1998; **63**: 3010.
24. Wierlacher S, Sander W, Liu MTH. *J. Am. Chem. Soc.* 1993; **115**: 8943.
25. Bonneau R, Liu MTH, Kim KC, Goodman JL. *J. Am. Chem. Soc.* 1996; **118**: 3829.
26. Shustov GV, Liu MTH, Rauk A. *J. Phys. Chem. A* 1997; **101**: 2509.
27. Moss RA, Merrer DC Moss RA, Merrer DC. *Chem. Commun.* 1997; 617.
28. Ford F, Yuzawa T, Platz MS, Matinger S, Fülscher M. *J. Am. Chem. Soc.* 1998; **120**: 4430.
29. Nigam M, Platz MS, Showalter BM, Toscano JP, Johnson R, Abbot SC, Kirchhoff MM. *J. Am. Chem. Soc.* 1998; **120**: 8055.
30. Moss RA, Yan S, Krogh-Jespersen K. *J. Am. Chem. Soc.* 1998; **120**: 1088.
31. Pezcacki JP, Wood PD, Gadosy TA, Lusztyk J, Warkenin J. *J. Am. Chem. Soc.* 1998; **120**: 8681.
32. Shustov GV, Liu MTH, Houk KN. *Can. J. Chem.* 1999; **77**: 540.
33. Bonneau R, Liu MTH. *J. Phys. Chem. A* 2000; **104**: 4115.
34. Page M, McIver JWJ. *J. Phys. Chem.* 1988; **88**: 922.
35. (a) Kato S, Morokuma K. *J. Chem. Phys.* 1980; **73**: 3900; (b) Kato S, Morokuma K. *J. Chem. Phys.* 1980; **72**: 206.
36. (a) Hohenberg P, Kohn W. *Phys. Rev. B* 1994; **136**: 864; (b) Kohn W, Sham L. *Phys. Rev. A* 1965; **140**: 1133; (c) Parr RG, Yang W. *International Series of Monographs on Chemistry 16: Density Functional Theory of Atoms and Molecules.* Oxford University Press: New York, 1989.
37. (a) Becke AD. *J. Chem. Phys.* 1993; **98**: 5648; (b) Stevens JP, Devlin FJ, Chablowski CF, Frisch MJ. *J. Phys. Chem.* 1994; **98**: 11623.
38. Hariharan PC, Pople JA. *Theor. Chim. Acta* 1973; **28**: 213.
39. Dunning TH Jr. *J. Chem. Phys.* 1989; **90**: 1007.
40. Cremer D. In *Encyclopedia of Computational Chemistry*, Vol. 3, Schleyer PvR, Allinger NL, Clark T, Gasteiger J, Kollman PA, Schaefer HF III, Schreiner PR (eds). Wiley: Chichester, 1998; 1706.
41. Raghavachari K, Trucks GW, Pople JA, Head-Gordon M. *Chem. Phys. Lett.* 1989; **157**: 479.
42. (a) Carpenter JE, Weinhold F. *J. Mol. Struct. (Theochem)* 1988; **169**: 41; (b) Reed AE, Weinstock RB, Weinhold F. *J. Chem. Phys.* 1985; **83**: 735; (c) Reed AE, Curtiss LA, Weinhold F. *Chem. Rev.* 1988; **88**: 899.
43. (a) Garrett BC, Truhlar DG. *J. Am. Chem. Soc.* 1979; **101**: 4534; (b) Issacson AD, Truhlar DG. *J. Chem. Phys.* 1982; **76**: 1380.
44. Liu Y-P, Lynch GC, Truong TN, Lu DH, Truhlar DG, Garrett BC. *J. Am. Chem. Soc.* 1993; **115**: 2408.
45. Truhlar DG, Isaacson AD, Garrett BC. In *Theory of Chemical Reaction Dynamics*, Baer M (ed). CRC Press: Boca Raton, FL, 1985; 65.
46. Miller WH. *Chem. Rev.* 1987; **87**: 19.
47. Miller WH. In *Tunneling*, Jortner J, Pullman B (eds). Reidel: New York, 1986; 91.
48. Kraka E, Gräfenstein J, Gauss J, He Y, Reichel F, Olsson L, Konkoli Z, He Z, Cremer D. COLOGNE 2000. University of Göteborg: Göteborg, 2000.
49. Frisch MJ, Trucks GW, Schlegel HB, Scuseri GE, Robb MA, Cheeseman JR, Zakrzewski VG, Montgomery Jr JA, Stratmann

RE, Burant JC, Dapprich S, Millam JM, Daniels AD, Kudin KN, Strain MC, Farkas O, Tomasi J, Barone V, Cossi M, Cammi R, Mennucci B, Pomelli C, Adamo C, Clifford S, Ochterski J, Petersson GA, Ayala PY, Cui Q, Morokuma K, Malick DK, Rabuck AD, Raghavachari K, Foresman JB, Cioslowski J, Ortiz JV Stefanov BB, Liu G, Liashenko A, Piskorz P, Komaromi I, Gomperts R, Martin RL, Fox DJ, Keith T, Al-Laham MA, Peng CY, Nanayakkara A, Gonzalez C, Challacombe M, Gill PMW, Johnson B, Chen W, Wong MW, Andres JL, Gonzalez C, Head-Gordon M, Replogle ES, Pople JA. Gaussian 98, Revision A.5. Gaussian: Pittsburgh, PA, 1998.

50. Steckler R, Chuang Y-Y, Coitino EL, Hu WP, Liu Y-P, Lynch GC, Nguyen KA, Jackels CF, Gu MZ, Rossi I, Fast P, Clayton S, Melissas VS, Garrett BC, Isaacson AD, Truhlar GD. POLYRATE, version 7.0. University of Minnesota: Minneapolis, MN, 1996.

